Comput Geosci (2015) 19:1251–1268
DOI 10.1007/s10596-015-9541-4

ORIGINAL PAPER

High order discontinuous Galerkin method for simulating miscible flooding in porous media

Jizhou Li[1] · **Beatrice Riviere**[1]

Received: 23 December 2014 / Accepted: 13 October 2015 / Published online: 29 October 2015

Abstract We present a high-order method for miscible displacement simulation in porous media. The method is based on discontinuous Galerkin discretization with weighted average stabilization technique and flux reconstruction post processing. The mathematical model is decoupled and solved sequentially. We apply domain decomposition and algebraic multigrid preconditioner for the linear system resulting from the high-order discretization. The accuracy and robustness of the method are demonstrated in the convergence study with analytical solutions and heterogeneous porous media, respectively. We also investigate the effect of grid orientation and anisotropic permeability using high-order discontinuous Galerkin method in contrast with cell-centered finite volume method. The study of the parallel implementation shows the scalability and efficiency of the method on parallel architecture. We also verify the simulation result on highly heterogeneous permeability field from the SPE10 model.

Keywords Porous media flow · Miscible displacement · High-order method · Discontinuous Galerkin · Flux reconstruction · Algebraic multigrid · Domain decomposition · Parallel computing · Heterogeneous permeability · Anisotropy · SPE10 model

✉ Beatrice Riviere
riviere@rice.edu

Jizhou Li
Jizhou.Li@rice.edu

[1] Rice University, Houston TX, USA

1 Introduction

In enhanced oil recovery, a polymer-based solvent is injected in the reservoir to help improve total production of hydrocarbon from the reservoir. Unlike immiscible fluids such as water that do not mixed with the residing hydrocarbon, the injected solvent mixes with the remaining oil, forming a single-phase fluid mixture that is further displaced throughout the reservoir.

The mathematical model that governs the displacement of the fluid mixture is known to be the miscible displacement equations. The problem consists of a system of partial differential equations (PDE) with pressure, velocity, and concentration as unknowns. The problem poses several numerical challenges. The PDE system itself is nonlinear. Input data, such as the permeability field, is discontinuous and varies with several orders in magnitude for realistic porous media.

Low-order methods such as finite difference and finite volume method have long been used to solve the miscible displacement problem. However, these methods suffer significantly from grid orientation [1, 2]. In order to properly simulate the fluid flow, many of these low-order methods , when used on unstructured meshes, require carefully constructed unstructured meshes [3], such as k-orthogonal grids. The constraint on griding of the computational domain can be significantly restrictive to accurately portrait the complex geometry of the subsurface formations.

Recently, there has been a significant interest generated in the study of high-order methods for porous media flow [4–6]. High-order methods are less restricted to the grid orientation and complex geometry. Methods such as discontinuous Galerkin (DG) methods are a popular choice for the fluid flow problem. The DG methods provide high-order accuracy while maintaining local mass-conservation. The

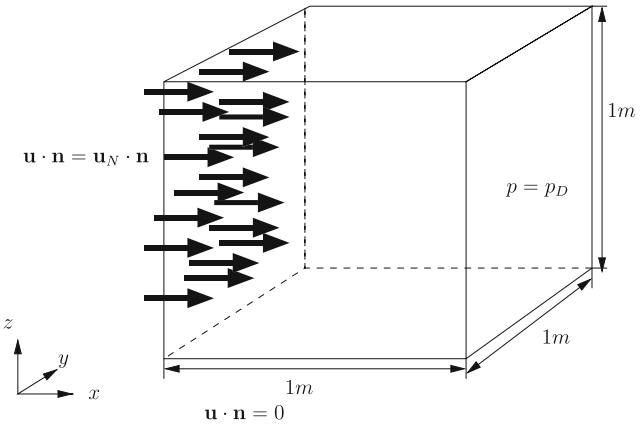

Fig. 1 Flux driven problem

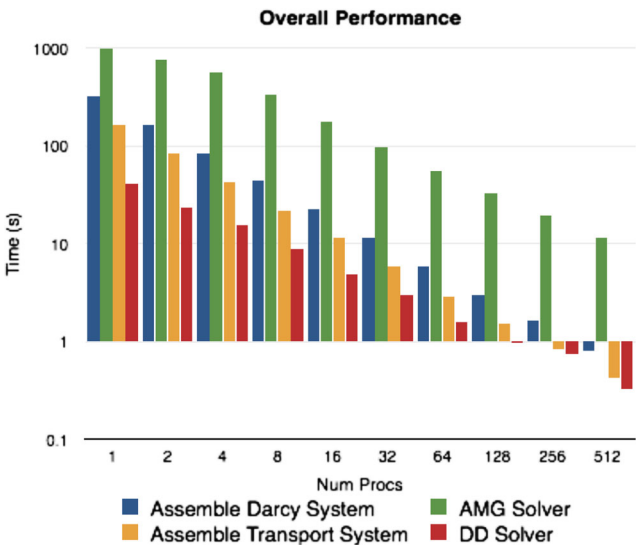

Fig. 3 Overall performance

idea of using discontinuous Galerkin methods for solving the miscible displacement problem is not new. In [7], the DG method is applied to two-dimensional media with mild heterogeneities. Theoretical convergence has been obtained for smooth solutions in [8]. The novelty of this paper is to show robustness and efficiency of a DG method for two- and three-dimensional media with realistic permeability fields. Our proposed method is based on the plain interior penalty discontinuous Galerkin method, studied in [7, 8], but it incorporates additional techniques to make it competitive for large scale computations.

We identify three challenges when using discontinuous Galerkin methods for solving porous media flow problems such as miscible displacement. A first challenge arises from highly heterogeneous permeabilities and flux reconstruction. As a consequence of using discontinuous polynomial approximations, the flux we obtain directly from taking the gradient of the pressure is not continuous in the normal direction across element boundaries. This can lead to numerical instabilities for heterogeneous media [9]. One approach to resolve the issue is to use a fully-implicit scheme to weakly impose the continuity of the flux in the coupled scheme [10, 11]. The fully-implicit scheme, however, can pose additional difficulties in solving the large nonlinear coupled system for pressure and concentration. A less costly method is the sequential approach that first solves the pressure and velocity from the Darcy system, and second the concentration from the transport system. Both pressure and velocity can be solved simultaneously by the locally mass conservative mixed finite element (MFE) method. This has the advantage of producing a continuous flux in the normal direction. The transport system is solved subsequently using DG [6, 12–15]. Mixed DG was

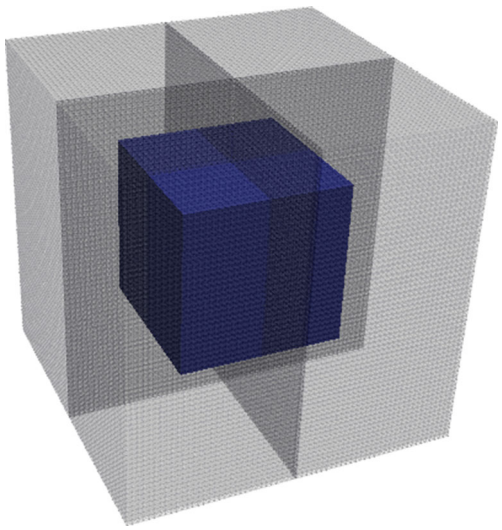

Fig. 2 Discontinuous permeability field

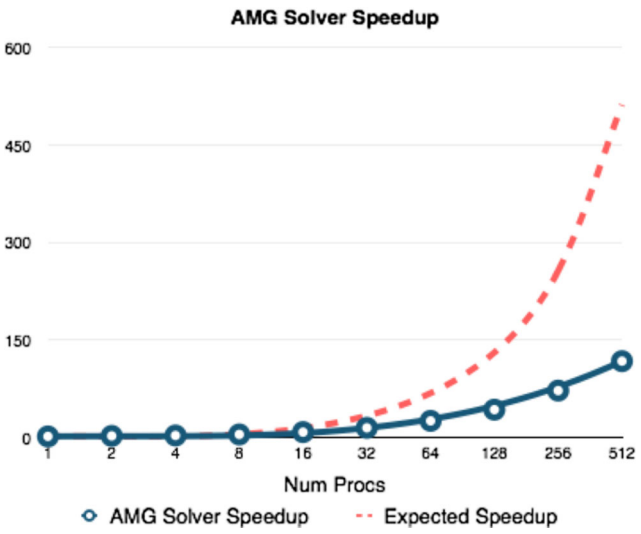

Fig. 4 AMG solver speedup

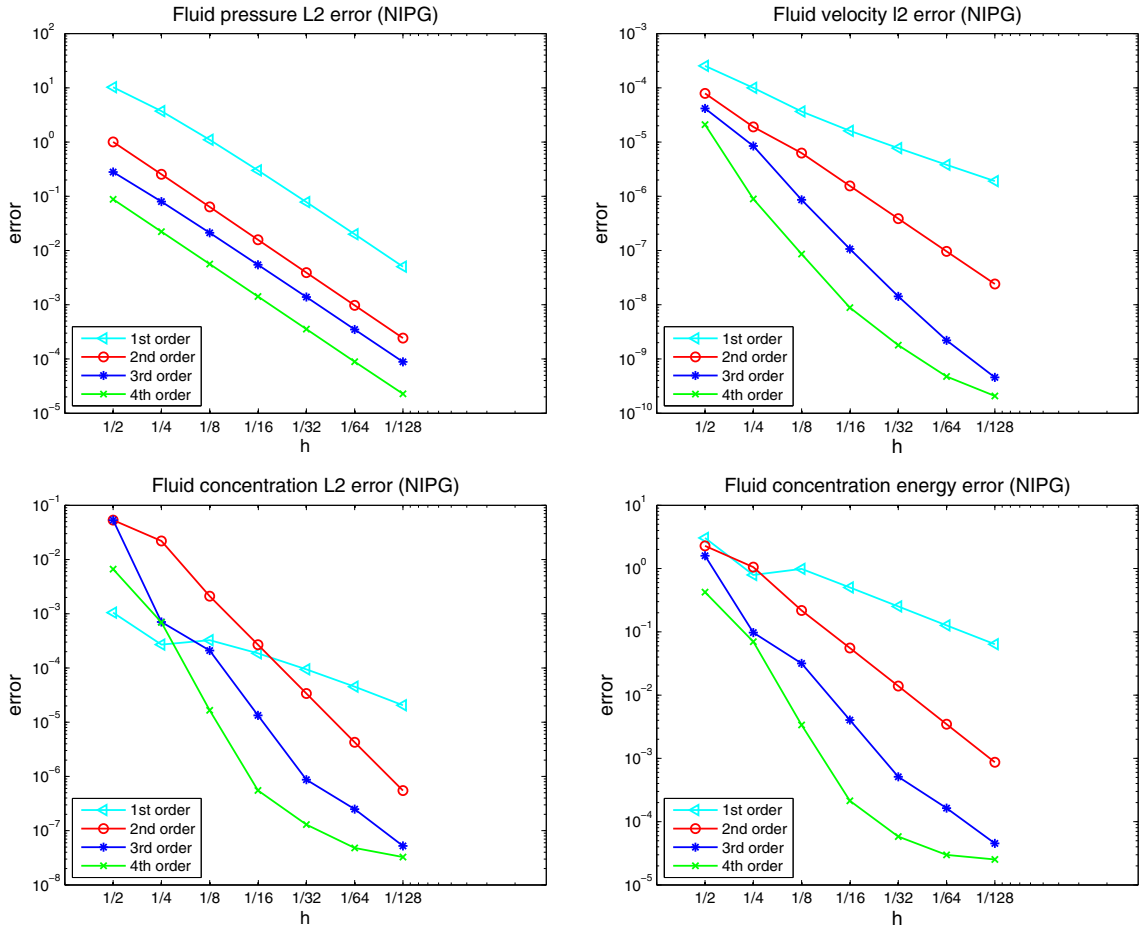

Fig. 5 Error in spatial discretization for first-, second-, third-, and fourth-order methods in space. A second order in time method is used

also introduced in [16] to impose continuity of the flux on the face weakly. For large scale simulations, however, the higher order mixed finite methods using either Raviart-Thomas (RT) basis of order two or three or Brezzi-Douglas-Marini (BDM) basis of order two or higher have rarely been used due to the complexity of generating the finite element space and the fact that hybridization is required for MFE to avoid solving large indefinite saddle-point systems. The method we propose uses discontinuous Galerkin method, with weighted average stabilization [17], for both the Darcy and transport systems. It allows for arbitrary order of approximation in space. The resulting discontinuous flux obtained by taking the gradient of the pressure has to be reconstructed, following approaches introduced in [9, 18]. The BDM flux reconstruction proposed in [9] has been used for single-phase flow in [19]. The RT flux reconstruction introduced in [18] has been used for two-phase flow [20–22]. In our method, we extend the reconstruction approach to the miscible displacement problem.

A second challenge arises from the linear solver. As the consequence of the high-order DG discretization and highly heterogeneous permeability for realistic simulations, the linear system resulting from the discretization is much more ill-conditioned than the system resulting from the low-order discretization. This issue is addressed by using a modified algebraic multigrid (AMG) preconditioner based on [23, 24]. We show that with domain decomposition and AMG preconditioning on parallel clusters, high-order discontinuous Galerkin method can be both efficient and accurate for simulating large scale porous media flow problems. Two-level AMG preconditioning of DG systems, in particular the selection of the subspaces for the coarsening step, is itself a subject of great interest. Conforming piecewise linear finite element, Crouzeix-Raviart non-conforming piecewise linear finite element and piecewise constant subspace corrections are indeed effective coarsening strategies for the smoothed aggregation AMG approach [25]. More recently, the work [26] demonstrates the feasibility and efficiency for piecewise constant subspace correction with smoothed aggregation AMG. But, to our knowledge, this type of subspace correction has not been used in the framework of non-smoothed aggregation AMG. In contrast with the

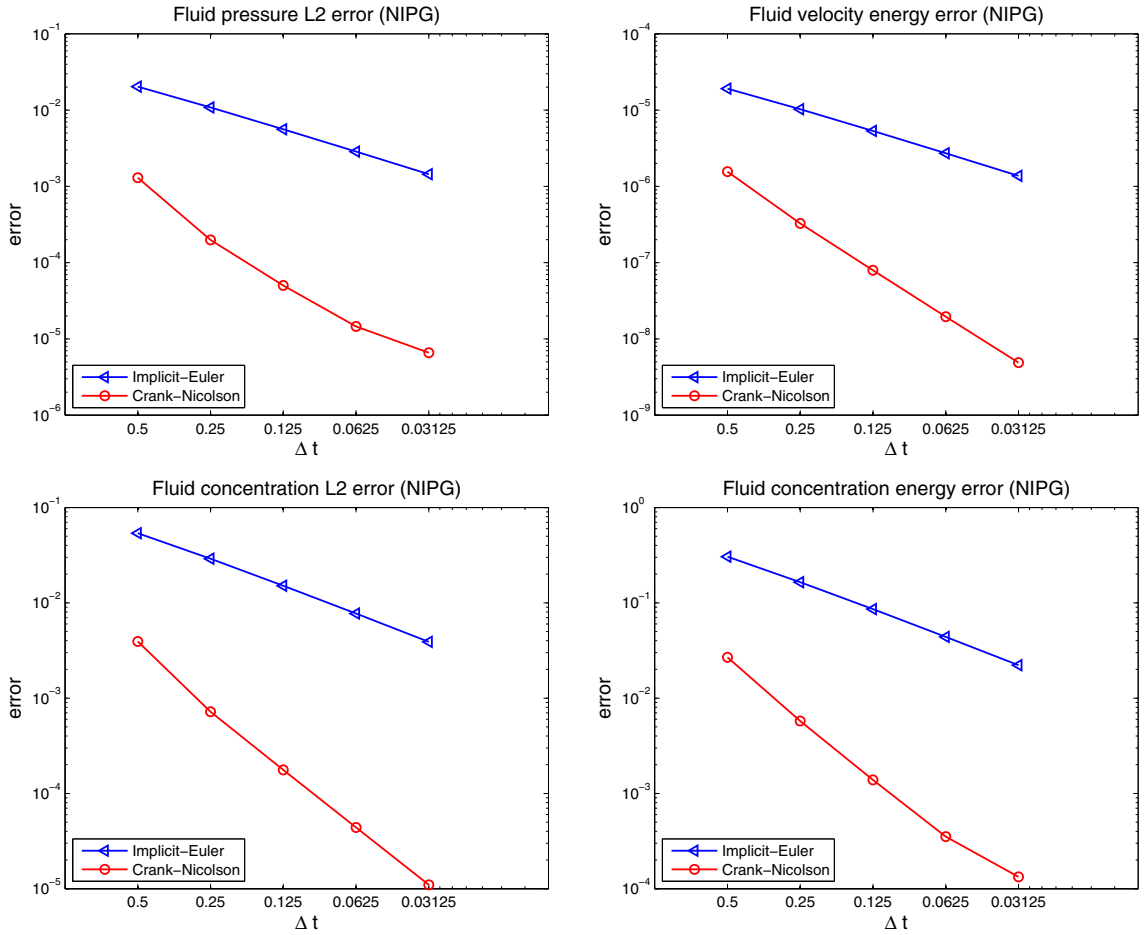

Fig. 6 Error in time updating for first- and second-order methods in time. A fourth-order method in space is used

non-smoothed aggregated AMG, the smoothed aggregated AMG produces additional fill-in on the coarser level. The effect is more obvious in the case with higher order approximation. Hence, it is suggested that non-smoothed aggregation AMG can be used for higher order DG with highly heterogeneous porous media. Blatt et al. [24] uses non-smoothed aggregation AMG with piecewise continuous linear subspace correction. The novelty in our work is to propose a piecewise constant subspace correction strategy for the non-smoothed aggregation AMG.

Finally, overshoot and undershoot phenomena occur in many high-order methods including mixed finite element or multi-point flux approximation [27]. The issue can be resolved using slope limiter [28–30]. However, in our simulations, overshoot and undershoot are sparse and less than 5 %, and thus, we do not use slope limiters. Our numerical examples show that our method can produce solutions of good quality.

The outline of the paper is as follows. After a brief description of the mathematical problem in Section 2, we introduce the semi-discrete scheme in Section 3. The coupling strategy is defined in Section 4. Section 5 addresses scalability of the AMG solver. Various numerical examples that test the convergence and robustness of our method are shown in Section 6. Conclusions follow.

2 Model problem

The displacement of the single phase fluid mixture in the porous medium $\Omega \subset \Re^d$ over a time interval $[0, T]$ is characterized by the following mathematical model:

$$\nabla \cdot \mathbf{u} = q^I - q^P, \quad \text{in} \quad \Omega \times (0, T), \tag{1}$$

$$\mathbf{u} = -\mathbf{K}(c)(\nabla p - \rho(c)\mathbf{g}), \quad \text{in} \quad \Omega \times (0, T), \tag{2}$$

$$\partial_t(\phi c) - \text{div}\,(\mathbf{D}(\mathbf{u})\nabla c - c\mathbf{u}) = q^I \hat{c} - q^P c, \quad \text{in} \quad \Omega \times (0, T), \tag{3}$$

where the physical unknowns are p the fluid pressure, $\mathbf{u}$ the velocity, and c the concentration of the solvent.

The flow and transport processes can be driven by the functions q^I and q^P which represent injection wells and production wells, respectively. The other coefficients in the system are the fluid density $\rho(c)$, the gravity vector $\mathbf{g}$, the

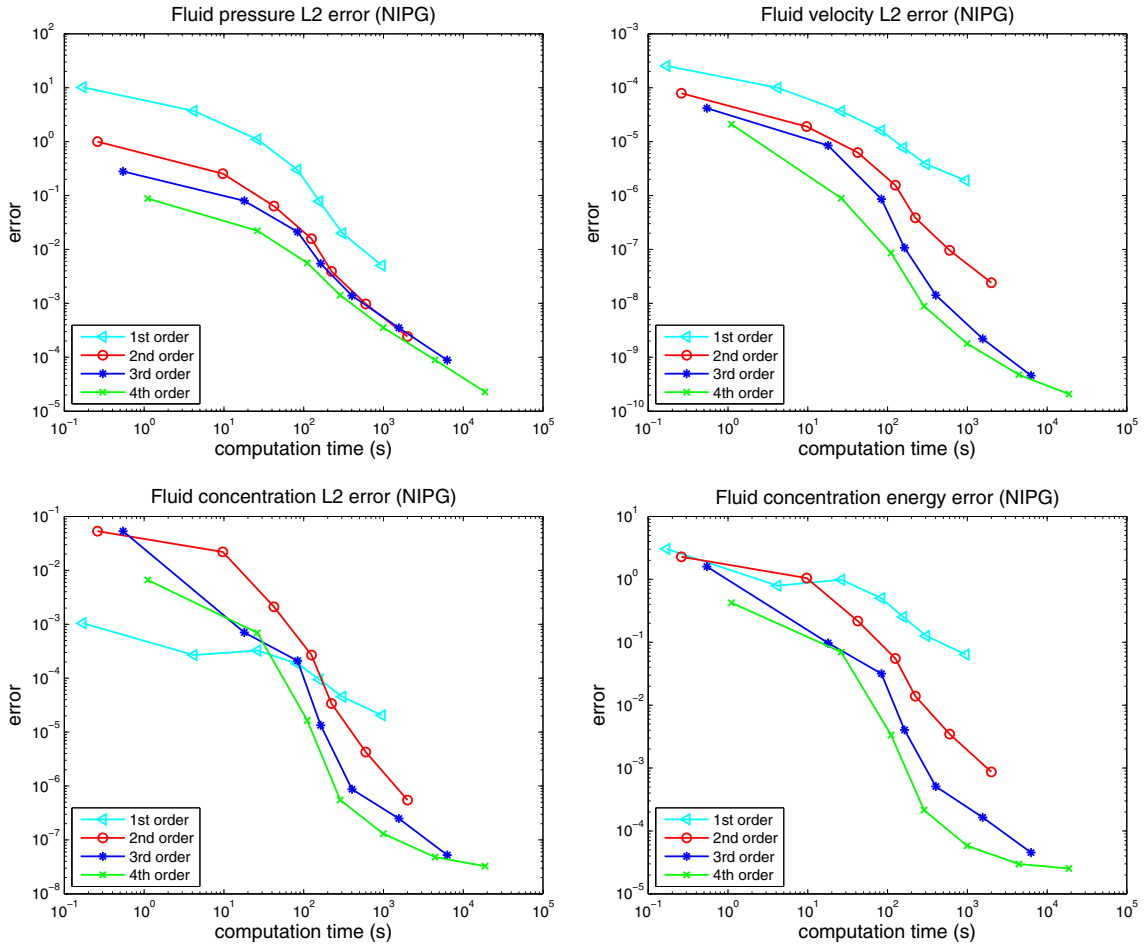

Fig. 7 Computation time vs. accuracy

porosity of the medium ϕ, the diffusion-dispersion matrix $\mathbf{D}(\mathbf{u})$, the injected concentration $\hat{c}$, and the matrix $\mathbf{K}(c)$, which is the product of the scalar $1/\mu(c)$ and the permeability matrix $\mathbf{k}$. The initial concentration is denoted by c_0.
Throughout the paper, we choose a commonly used form for the fluid mixture density

$$\rho(c) = c\rho_s + (1-c)\rho_o,$$

where ρ_s is the density for the fluid used to displace the residing fluid with density ρ_o [31]. The diffusion-dispersion tensor is based on the semi-empirical relation [12],

$$\mathbf{D}(\mathbf{u}) = d_m\mathbf{I} + |\mathbf{u}|\,(\alpha_l\mathbf{E}(\mathbf{u}) + \alpha_t(\mathbf{I} - \mathbf{E}(\mathbf{u}))),$$

where $\mathbf{E}(\mathbf{u}) = \mathbf{u}\mathbf{u}^T\,|\mathbf{u}|^{-2}$. The parameter d_m is associated with molecular diffusion; α_l is the longitudinal dispersivity and α_t is the transverse dispersivity.
For the viscosity, we will use the quarter mixing rule [32],

$$\mu(c) = (c\mu_s^{-0.25} + (1-c)\mu_o^{-0.25})^{-4},$$

where μ_s is viscosity of the solvent and μ_o is viscosity of residing fluid. We complete the system by the boundary conditions:

$$p = p_D \text{ on } \Gamma_D, \quad \mathbf{u}\cdot\mathbf{n} = \mathbf{u}_N\cdot\mathbf{n} \text{ on } \Gamma_N,$$
$$\text{and} \quad c = c_{in} \text{ on } \Gamma_{in}, \quad \mathbf{D}(\mathbf{u})\nabla c\cdot\mathbf{n} = q_{out} \text{ on } \Gamma_{out}.$$

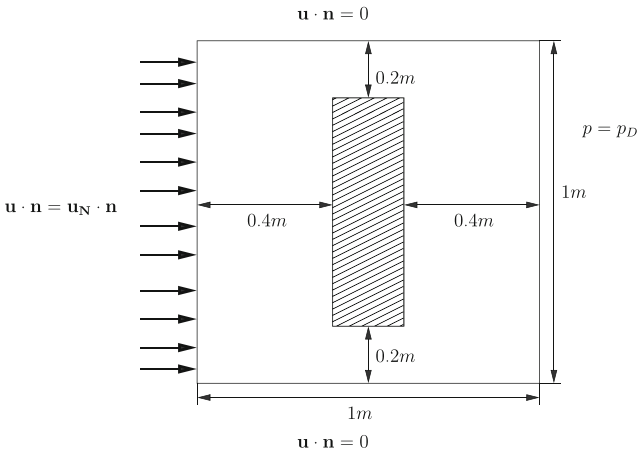

Fig. 8 2D flux driven problem with lens

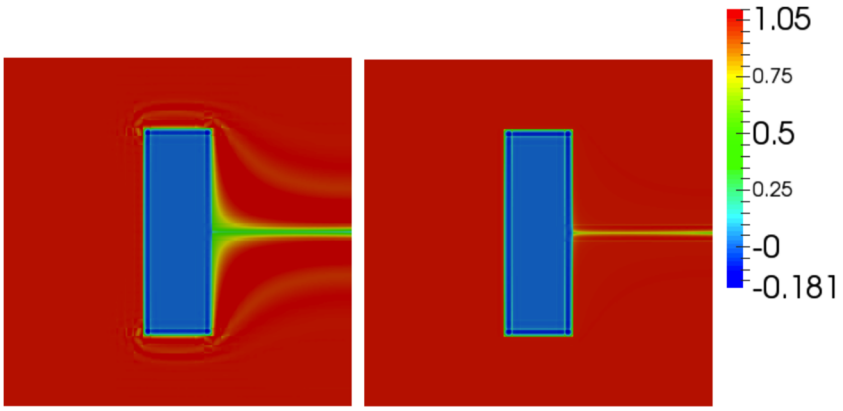

Fig. 9 Concentration profile with DG2 on 40 × 40 Cartesian grid: no flux reconstruction (*left*) and with flux reconstruction (*right*)

If the boundary condition is set to be no flow boundary condition, i.e., $\Gamma_N = \partial\Omega$, then we have to complete the system by an additional constraint on the pressure for uniqueness and we also need a compatibility condition,

$$\int_{\partial\Omega} \mathbf{u}_N \cdot \mathbf{n} = \int_{\Omega} (q^I - q^P).$$

3 Spatial discretization

Let $\{\mathcal{E}_h\}_{h>0}$ be a regular family of meshes of Ω, where h is the maximum element diameter and let Γ_h denote the set of all the interior faces of the mesh $\mathcal{E}_h$. We fix a unit normal vector $\mathbf{n}_e$ for each interior face and denote by E^e_+ and E^e_- the elements in $\mathcal{E}_h$ such that $e = \partial E^e_+ \cap \partial E^e_-$ and $\mathbf{n}_e$ points from E^e_+ to E^e_-. Then, we define the average and jump on the face e to be,

$$\{v\} = \frac{1}{2} v|_{E^e_+} + \frac{1}{2} v|_{E^e_-}, \quad \text{and} \quad [v] = v|_{E^e_+} - v|_{E^e_-}.$$

The weighted average $\{\cdot\}_\omega$ is defined, with the weights $\omega_{E^e_+}$ and $\omega_{E^e_-}$

$$\{v\}_\omega = \omega_{E^e_+} v|_{E^e_+} + \omega_{E^e_-} v|_{E^e_-}, \quad \text{and} \quad \omega_{E^e_+} + \omega_{E^e_-} = 1.$$

If e is a boundary face, then the average and jump are defined as

$$\{v\} = v, \quad \text{and} \quad [v] = v.$$

We use $(\cdot,\cdot)$ to denote the standard L^2 inner product over the entire domain. For the broken Sobolev spaces, we define the L^2 inner-product on $\mathcal{E}_h$ and Γ_h to be:

$$(\cdot,\cdot)_{\mathcal{E}_h} = \sum_{E\in\mathcal{E}_h} (\cdot,\cdot)_E, \qquad (\cdot,\cdot)_{\Gamma_h} = \sum_{e\in\Gamma_h} (\cdot,\cdot)_e.$$

3.1 Discretization of pressure equation

Now, we can define the DG discretization for the pressure equation obtained by combining (1) and (2)

$$B_d(p_h, q_h; c_h) = \ell_d(q_h; c_h), \tag{4}$$

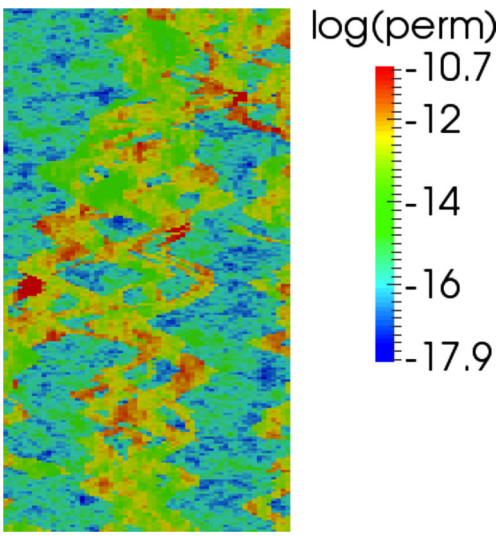

Fig. 10 SPE10 permeability: layer 39 (log scale)

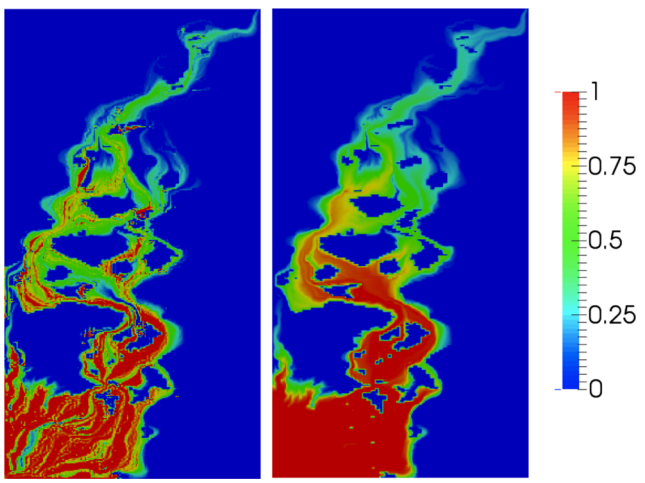

Fig. 11 Concentration profile after 13 days, obtained with second-order method: no flux reconstruction (*left*) and with flux reconstruction (*right*)

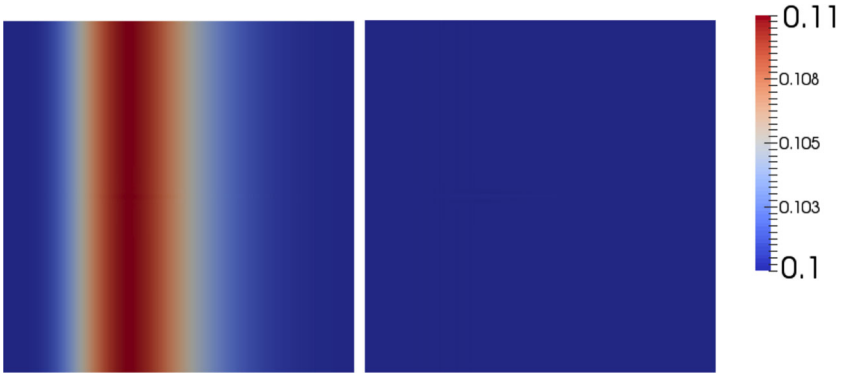

Fig. 12 Velocity in x-direction with -G2 on 80×80 Cartesian grid

where

$$\begin{aligned} B_d(p_h, q_h; c_h) \;=\; & (\mathbf{K}(c_h)(\nabla p_h - \rho(c_h)\mathbf{g}), \nabla q_h)_{\mathcal{E}_h} \\ & + \left(\sigma \gamma_e h_e^{-1}[p_h], [q_h]\right)_{\Gamma_h \cup \Gamma_D} \\ & - ([q_h], \{\mathbf{K}(c_h)(\nabla p_h - \rho(c_h)\mathbf{g}) \cdot \mathbf{n}_e\}_\omega)_{\Gamma_h \cup \Gamma_D} \\ & + \epsilon_1 ([p_h], \{\mathbf{K}(c_h)\nabla q_h \cdot \mathbf{n}_e\}_\omega)_{\Gamma_h \cup \Gamma_D}. \end{aligned}$$

The right-hand side is defined as,

$$\begin{aligned} \ell_d(q_h; c_h) \;=\; & \left(q^I - q^P, q_h\right) - (\mathbf{u}_N \cdot \mathbf{n}_e, q_h)_{\Gamma_N} \\ & + \left(\sigma \gamma_e h_e^{-1} p_D, q_h\right)_{\Gamma_D} \\ & + \epsilon_1 (\mathbf{K}(c_h)\nabla q_h \cdot \mathbf{n}_e, p_D)_{\Gamma_D}. \end{aligned}$$

The pressure, concentration, and their corresponding test functions are in the following finite-dimensional subspaces:

$$P_h = \{q_h \in L^2(\Omega) : q_h|_E \in \mathcal{P}_k(E), E \in \mathcal{E}_h\},$$
$$C_h = \{c_h \in L^2(\Omega) : c_h|_E \in \mathcal{P}_r(E), E \in \mathcal{E}_h\}.$$

Here, $\mathcal{P}_k(E)$ denotes the space of polynomials of degree less than or equal to k over the element E.

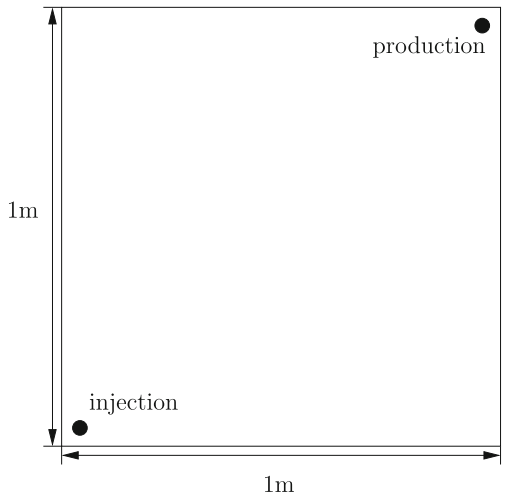

Fig. 13 Quarter five-spot problem set-up

The parameter ϵ_1 is set to be either -1, 0 or 1. This will yield symmetric interior penalty Galerkin (SIPG), incomplete interior penalty Galerkin (IIPG), or non-symmetric penalty Galerkin (NIPG) method, respectively.

For the weights in the weighted average, we first define,

$$\delta_e^+ = \mathbf{K}^+(\tilde{c}_h^+)\mathbf{n}_e \cdot \mathbf{n}_e \text{ and } \delta_e^+ = \mathbf{K}^-(\tilde{c}_h^-)\mathbf{n}_e \cdot \mathbf{n}_e,$$

where $\tilde{c}_h$ is taken to be the concentration evaluated at the center of the cell. Hence, the weights are constructed as

$$\omega_{E_+^e} = \delta_e^-(\delta_e^+ + \delta_e^-)^{-1} \text{ and } \omega_{E_-^e} = \delta_e^+(\delta_e^+ + \delta_e^-)^{-1},$$

and the penalty term is chosen as [33]

$$\gamma_e = 2\delta_e^+\delta_e^-(\delta_e^+ + \delta_e^-)^{-1}k(k+d-1).$$

The term h_e is given by

$$h_e = |e|^{-1} \min\left(\left|E^+\right|, \left|E^-\right|\right).$$

The multiplicative factor σ in the penalty term is constant and chosen equal to one in our simulations.

3.2 Flux reconstruction

Flux reconstruction methods have been proposed to improve the accuracy of the DG velocity, in particular for heterogeneous media. In Section 6.2, we compare various numerical solutions obtained with and without flux reconstruction. We employ the Raviart-Thomas (RT) flux reconstruction approach proposed by Ern et al. [18]. We recall below the flux reconstruction method for triangular elements. The DG velocity, obtained directly from DG discretization of the pressure, is projected onto the Raviart-Thomas space, denoted by $\mathbf{U}_h$.

$$\mathbf{U}_h = \{\mathbf{u}_h \in H(\Omega; \text{div}) \,|\, \mathbf{u}_h|_E \in (\mathcal{P}_k(E))^2 + \mathbf{x}\mathcal{P}_k(E),\, E \in \mathcal{E}_h\}.$$

Let $\mathbf{u}_h \in \mathbf{U}_h$ denote the reconstructed flux. It is defined locally on each element E by:

$$(\mathbf{u}_h, \mathbf{v}_h)_E = \left(\mathbf{u}_h^{DG}, \mathbf{v}_h\right)_E + \epsilon_1 \textstyle\sum_{e \in \partial E} \omega_{E^e}(\mathbf{K}(c_h)\mathbf{v}_h \cdot \mathbf{n}_e, [p_h])_e, \quad (5)$$
$$(\mathbf{u}_h \cdot \mathbf{n}_e, q_h)_e = \left(\left\{\mathbf{u}_h^{DG}\right\}_\omega \cdot \mathbf{n}_e + \sigma \gamma_e h_e^{-1}[p_h], q_h\right)_e, \quad \forall e \in \partial E, \quad (6)$$

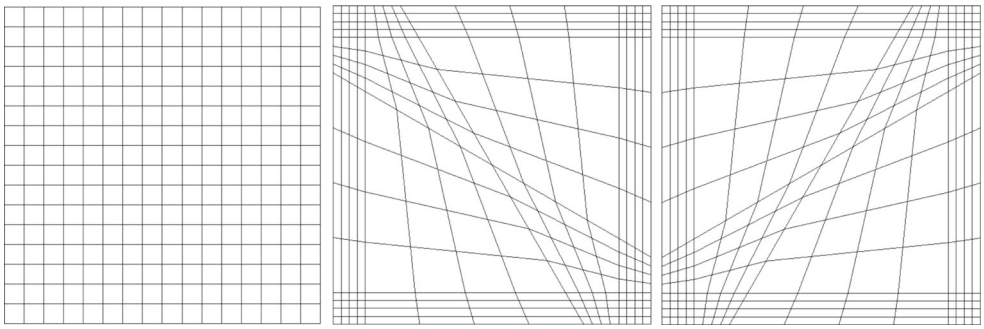

Fig. 14 Meshes for grid distortions study: no distortion (*left*), 30° distortion (centre), −30° distortion (*right*)

with $q_h \in \mathcal{P}_k(e)$ and $\mathbf{v}_h \in (\mathcal{P}_{k-1}(E))^2$, and with

$$\mathbf{u}_h^{DG} = -\mathbf{K}(c_h)(\nabla p_h - \mathbf{g}\rho(c_h)).$$

We note that the penalty term in the right-hand side of Eq. 6 is needed for maintaining mass conservation. We also generalize the projection for quadrilateral elements by defining the space $\mathbf{U}_h$ as

$$\mathbf{U}_h = \{\mathbf{u}_h \in H(\Omega; \mathrm{div}) | \mathbf{u}_h|_E \in Q_{k+1,k}(E) \times Q_{k,k+1}(E), E \in \mathcal{E}_h\},$$

and

$$Q_{l,m}(E) = \left\{ \phi : \phi(\mathbf{x}) = \sum_{i=0}^{l} \sum_{j=0}^{m} \alpha_{i,j} \mathbf{x}_1^i \mathbf{x}_2^j, \mathbf{x} \in E, \alpha_{i,j} \in \Re \right\}.$$

The flux reconstruction is given the same as Eqs. 5 and 6 with $q_h \in \mathcal{P}_k(e)$ and $\mathbf{v}_h \in Q_{k-1,k}(E) \times Q_{k,k-1}(E)$. The projection can also be extended to three-dimensional elements. The projection is an element-wise post-processing, therefore, not computationally expensive. Typically, the order of the space $\mathbf{U}_h$ is chosen consistently with the order of the pressure space P_h.

3.3 Discretization of concentration equation

We now proceed to define the DG discretization of the transport Eq. 3 that utilizes the projected velocity $\mathbf{u}_h$.

First, we discretize the diffusion term $-\mathrm{div}(\mathbf{D}(\mathbf{u})\nabla c)$ as follow.

$$\begin{aligned} B_{di}(c_h, w_h; \mathbf{u}_h) = & (\mathbf{D}(\mathbf{u}_h)\nabla c_h, \nabla w_h)_{\mathcal{E}_h} \\ & -(\{\mathbf{D}(\mathbf{u}_h)\nabla c_h \cdot \mathbf{n}_e\}_\omega, [w_h])_{\Gamma_h \cup \Gamma_{in}} \\ & +\epsilon_2(\{\mathbf{D}(\mathbf{u}_h)\nabla w_h \cdot \mathbf{n}_e\}_\omega, [c_h])_{\Gamma_h \cup \Gamma_{in}} \\ & + \left(\sigma \gamma_e h_e^{-1}[c_h], [w_h]\right)_{\Gamma_h \cup \Gamma_{in}}. \end{aligned}$$

The construction of the weighted average and other related terms is similar to the DG discretization of the Darcy system.

Now, for the convection-source term $\mathrm{div}(c_h \mathbf{u}_h) + q^P c_h$, we define:

$$\begin{aligned} B_{cq}(c_h, w_h; \mathbf{u}_h) = & -(c_h \mathbf{u}_h, \nabla w_h)_{\mathcal{E}_h} + (c_h^{\mathrm{up}} \mathbf{u}_h \cdot \mathbf{n}_e, [w_h])_{\Gamma_h \cup \Gamma_{out}} \\ & + (q^P c_h, w_h), \end{aligned}$$

where the upwind term is given as

$$c_h^{\mathrm{up}} = \begin{cases} c_h|_{E_+^e} & \text{if } \mathbf{u}_h \cdot \mathbf{n}_e > 0, \\ c_h|_{E_-^e} & \text{if } \mathbf{u}_h \cdot \mathbf{n}_e \le 0. \end{cases}$$

We then set

$$B_{tr}(c_h, w_h; \mathbf{u}_h) = B_{di}(c_h, w_h; \mathbf{u}_h) + B_{cq}(c_h, w_h; \mathbf{u}_h).$$

For the right-hand side, we have

$$\begin{aligned} \ell_{tr}(w_h; \mathbf{u}_h) = & (q_{out}, w_h)_{\Gamma_{out}} + (q^I \hat{c}, w_h) - (c_{in} \mathbf{u}_h \cdot \mathbf{n}_e, w_h)_{\Gamma_{in}} \\ & + \epsilon_2 (\mathbf{D}(\mathbf{u}_h)\nabla w_h \cdot \mathbf{n}_e, c_{in})_{\Gamma_{in}} + \left(\sigma \gamma_e h_e^{-1} c_{in}, w_h\right)_{\Gamma_{in}}. \end{aligned}$$

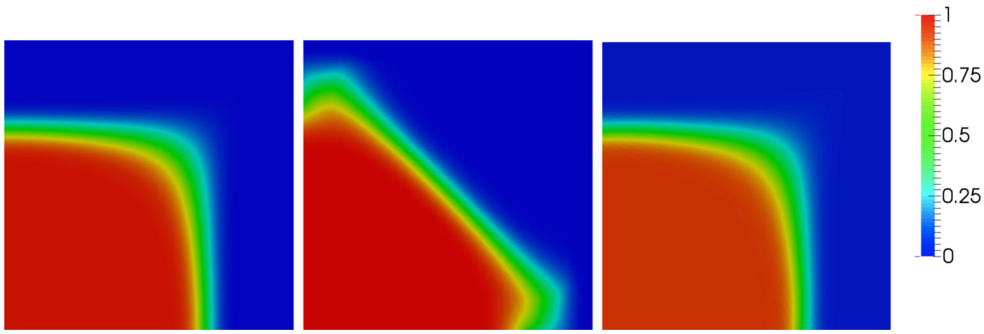

Fig. 15 Concentration profiles on grid with 30° distortion: CCFV reference (*left*), CCFV on h5 (centre), DG1 on h3 (*right*)

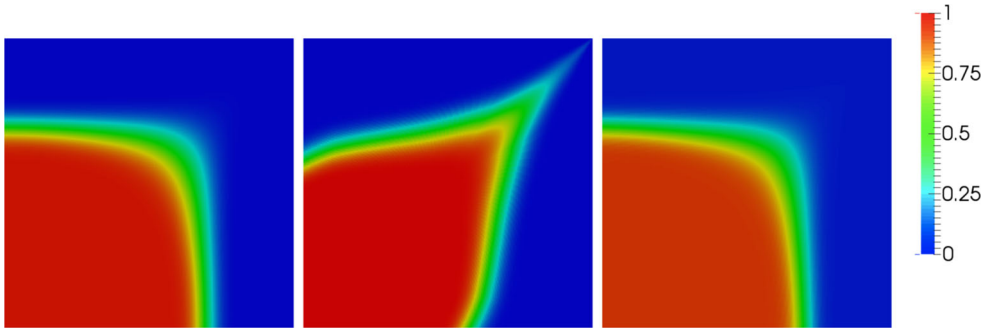

Fig. 16 Concentration profiles on grid with $-30°$ distortion: CCFV reference (*left*), CCFV on h5 (center), DG1 on h3 (*right*)

Hence, the semi-discrete formulation for the transport system becomes:
for all $t > 0$ the solution $c_h(t) \in C_h$ satisfies

$$(\phi \partial_t c_h, w_h) + B_{tr}(c_h, w_h; \mathbf{u}_h) = \ell_{tr}(w_h; \mathbf{u}_h), \qquad (7)$$
$$(c_h(0), w_h) = (c_0, w_h),$$

for all $w_h \in C_h$.

4 Fully-discrete scheme and decoupling algorithm

We solve the system (4) and (7) sequentially. This decoupling approach is advantageous over the fully implicit scheme with respect to computational cost. In addition, physical evidence has shown that the pressure does not vary as rapidly as the concentration, and the cost can be further reduced by taking larger time steps for the pressure than for the concentration [34].

Let $\{t_j\}_{j=0}^N$ be a regular time step partition of time interval $[0, T]$. The time step is denoted by $\Delta t_j = t_{j+1} - t_j$. The solutions at time t_j are denoted p_h^j, c_h^j, and $\mathbf{u}_h^j$. We use implicit Euler or Crank-Nicolson updating for the transport equation.

Now, we present our proposed algorithms for solving the miscible displacement problem.

Algorithm 1 Implicit Euler Decoupling Algorithm

Data: Initial condition, boundary condition, well information, etc.
initialize $t_0 = 0; \Delta t_0; c_h^0$;
while $j = 0 : N$ **do**
  Solve Darcy system for p_h^j with given c_h^j;
  Reconstruct velocity $\mathbf{u}_h^j$ based on p_h^j and c_h^j;
  Solve transport system for c_h^{j+1} with given $\mathbf{u}_h^j$ with Implicit Euler;
  $t_{j+1} = t_j + \Delta t_j$;
end

For higher order approximation in time with Crank-Nicolson method, the algorithm is given based on [14].

Algorithm 2 Crank-Nicolson Decoupling Algorithm

Data: Initial condition, boundary condition, well information, etc.
initialize $t_0 = 0; \Delta t_0; c_h^0$;
Set $c_h^{(0)} = c_h^0$;
Compute c_h^1 using Implicit Euler algorithm over $[0, \Delta t_0]$;
for $j = 1 : N$ **do**
  Solve Darcy system for p_h^j with given c_h^j;
  Reconstruct velocity $\mathbf{u}_h^j$ based on p_h^j and c_h^j;
  Compute $\hat{\mathbf{u}}_h^{j+1} = \frac{3}{2}\mathbf{u}_h^j - \frac{1}{2}\mathbf{u}_h^{j-1}$;
  Solve transport system for c_h^{j+1} with given $\hat{\mathbf{u}}_h^{j+1}$ using Crank-Nicolson;
  $t_{j+1} = t_j + \Delta t_j$;
end

The extrapolated velocity $\hat{\mathbf{u}}_h^{j+1}$ is needed to maintain the second-order convergence rate in time [35]. For other types

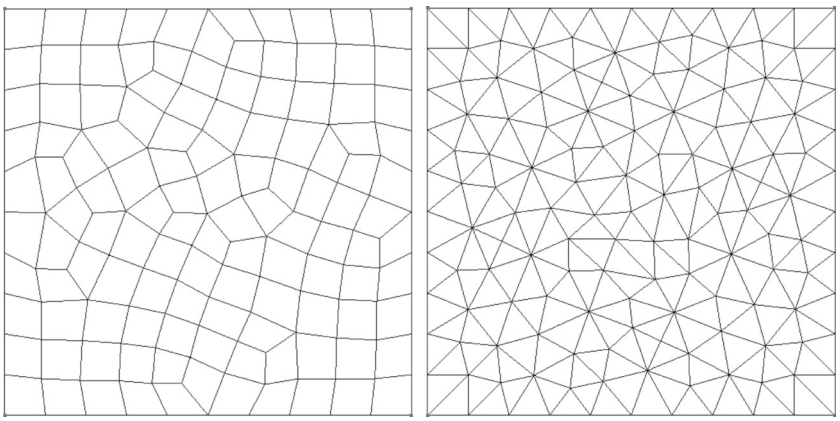

Fig. 17 Unstructured quadrilateral (*left*) and triangular (*right*) meshes

of high-order sequential time updating scheme, we refer readers to the algorithm in [6].

5 AMG preconditioner and overlapping domain decomposition

The Darcy system (4) resulting from the pressure equation is more difficult to solve than the transport system (7) because of the highly varying permeability field. Overlapping domain decomposition is used for the transport problem; each block is preconditioned by ILU(0) and solved by restarted GMRES.

For the Darcy system, we construct our preconditioner using algebraic multigrid (AMG) algorithm based on the works [23, 24]. Without going into the details of the solver, we give an overview of our approach for the reader familiar with AMG. We use overlapping domain decomposition for the parallel implementation and subspace correction to reduce the first coarse level onto low-order finite element space. The resulting coarser levels are constructed and solved by going through a V-cycle using non-smooth aggregation AMG. The coarsest level is solved using direct solver. We choose ILU(1) to be the smoother for the original system (4). On the coarse level, SSOR is used as smoother. Our approach differs from [23] by the choice of nonconforming piecewise constant for the low-order finite element space instead of continuous piecewise linears. We have observed that this choice results in a more robust solver for highly heterogeneous porous media. For the reduction onto the piecewise constant space, the restrictive operator can be constructed as follows

$$\psi_{E_i} = \sum_{E_i \in \mathcal{E}_h} \sum_j \mathbf{R}_{E_i,j} \phi_{E_i,j},$$

with

$$\phi_{E_i,j} \in P_h \text{ and } \psi_{E_i} = \begin{cases} 1 & \text{on } E_i, \\ 0 & \text{elsewhere.} \end{cases}$$

Then the restrictive operator is

$$\mathbf{R}_0 = \begin{pmatrix} \mathbf{R}_{E_1} & \mathbf{0} & \cdots & \mathbf{0} \\ \mathbf{0} & \mathbf{R}_{E_2} & \cdots & \mathbf{0} \\ \vdots & \vdots & \ddots & \vdots \\ \mathbf{0} & \mathbf{0} & \cdots & \mathbf{R}_{E_n} \end{pmatrix}.$$

The first coarse level can be constructed as

$$\mathbf{A}_0 = \mathbf{R}_0 \mathbf{A}_{DG} \mathbf{R}_0^T,$$

where $\mathbf{A}_{DG}$ is the linear system from (4). BiCGStab is used to solve the preconditioned system. We point out that $\mathbf{A}_0$ corresponds to cell-centered finite volume with harmonic averaging up to a constant (the penalty parameter) due to the weighted averages of [17].

To demonstrate the efficiency and the robustness of the solver, we consider a problem driven by flux boundary conditions at one side (velocity is 0.1 m/s), pressure on the other side ($p_D = 1000$ Pa), and no-flow boundary condition on the rest of the boundary, as illustrated in Fig. 1. Viscosities are chosen as

$$\mu_s = 5.8 Pa \cdot s \text{ and } \mu_o = 2.9 Pa \cdot s \tag{8}$$

Throughout the rest of the paper, the following parameters for the diffusion-dispersion matrix and porosity are fixed

$$d_m = 1.8 \times 10^{-7} m^2/s\ ,\ \alpha_l = 1.8 \times 10^{-5} m \text{ and}$$
$$\alpha_t = 1.8 \times 10^{-6} m, \quad \phi = 0.2. \tag{9}$$

The permeability field, as illustrated in Fig. 2, is discontinuous; the lens inside the domain have permeability equal to $10^{-4} m^2$ while the rest of the domain has permeability equal to $1 m^2$. The gravitational effect is neglected. The grid Peclet number is 10^4.

We have implemented the discretization in parallel architecture IBM iDataPlex with Intel(R) Xeon(R) CPU X5660 2.80 GHz processors. In Fig. 3, we present the performance of the entire simulation for one time step up to 512 processors with piecewise quadratic approximation ($\mathbb{Q}_2$ for the pressure and $\mathbb{P}_2$ for the concentration). The mesh contains 262,114 cells (cubes) which yields 7,077,078 degrees of freedom for the Darcy system and 2,621,140 degrees of freedom for the transport system.

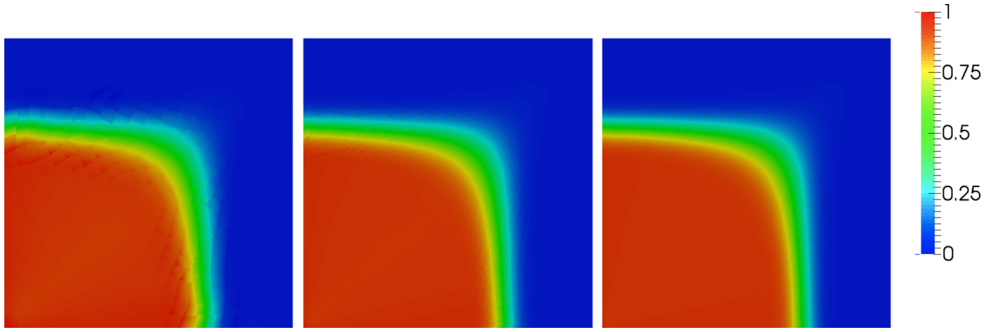

Fig. 18 Convergence of DG1 solutions on successively refined quadrilateral meshes: levels 1, 2, and 3

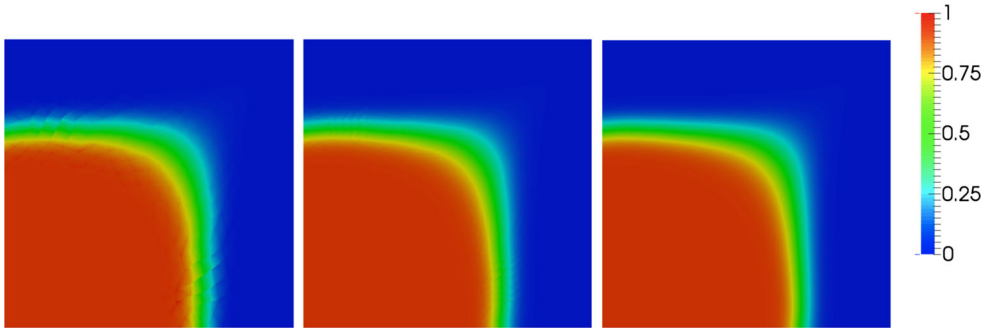

Fig. 19 Convergence of DG1 solutions on successively refined triangular meshes: levels 1, 2, and 3

Figure 3 shows the computational time for different aspects of the solver, in a strong scaling set-up. The most time-consuming process is the AMG solver for the Darcy system. Coarsening time is included in the speedup. This cost increases with the heterogeneities and discontinuities of the permeability field. Our proposed AMG solver performs well on the parallel cluster. Figure 4 suggests strong scalability of the AMG solver.

The implementation was done within Distributed and Unified Numerics Environment (DUNE) [36, 37] and DUNE-PDELab [38]. The flexible C++ template based development environment allows for an efficient implementation of our method.

6 Numerical results

6.1 Convergence study

First, we conduct study on the convergence of the discretization by testing the method with the following analytic solutions over the unit square

$$p(x, y, t) = (2+(-e^{-x}(1 + x + x^2) - e^{-y}(1 + y + y^2)))e^{\frac{\pi t}{2}},$$
$$c(x, y, t) = 0.5(\sin(2\pi x)^2 + \cos(2\pi y)^2)\sin(0.5\pi t).$$

The permeability is constant, $\mathbf{k} = 9.44 \times 10^{-3} m^2$, gravity is neglected and the viscosities are given by Eq. 8. We plot the L^2 norm of the errors in pressure, velocity, and concentration, and the broken H_0^1 norm of the errors in concentration. We vary the order of the spatial discretization from one to four. Crank-Nicolson updating is used with $T = 0.5$ s and a uniform time step $\Delta t = 0.001$ s (Fig. 5).

We observe, as expected, a higher convergence rate and a greater accuracy as the order of the method increases. Next, we test the convergence in time by fixing spatial order (four) and grid (size $h = 1/128$). Figure 6 demonstrates optimal rates in time for both implicit Euler and Crank-Nicolson decoupled algorithms.

We remark that for smooth solutions the Crank-Nicolson scheme yields second-order approximation in time. However, we have observed that for non-smooth realistic solutions, important overshoot and undershoot phenomena (about 10 %) occur in the neighborhood of a sharp gradient. Slope limiters are needed to minimize the overshoot/undershoot amounts even if they remain bounded throughout the simulation. For the remainder of the paper, we choose to use the implicit Euler scheme as overshoot/undershoot phenomena are negligible.

We also investigate the computational time required in order to achieve a given accuracy. We vary the order of

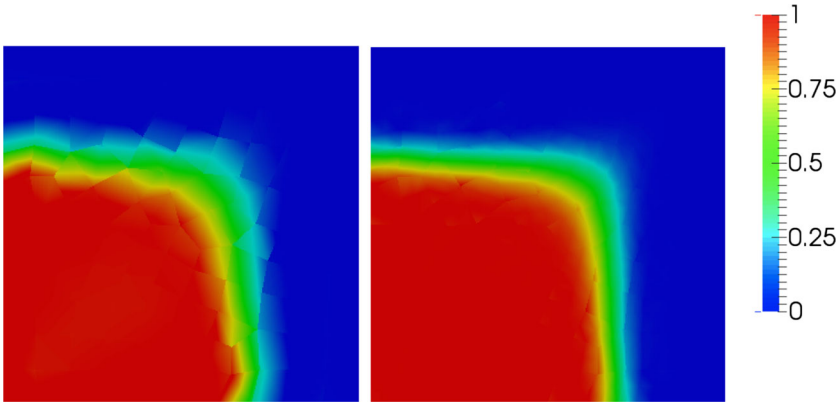

Fig. 20 p-Convergence of DG solutions on coarse quadrilateral mesh: $k = r = 1$ (*left*) and $k = r = 2$ (*right*)

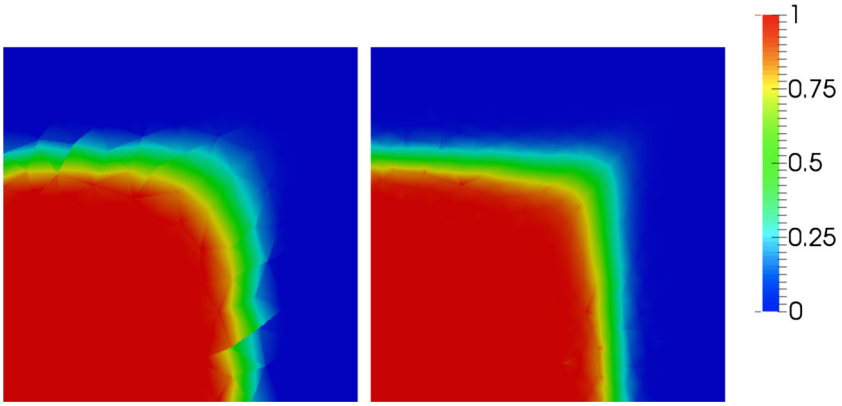

Fig. 21 p-Convergence of DG solutions on coarse triangular mesh: $k = r = 1$ (*left*) and $k = r = 2$ (*right*)

the method as well as the mesh size. Results are shown in Fig. 7.

From the results, we see that choosing a higher order method on a coarse mesh can not only yield greater accuracy but can also be faster than a lower order method on a finer mesh. The experiment is run in serial on Intel(R) Xeon(R) CPU X5660 2.80 GHz.

6.2 Effect of flux reconstruction

In this part, we investigate the impact of flux reconstruction, more specifically how it improves the quality of the solution. First, we consider a simple 2D case with flux driven flow for a discontinuous permeability ($10^{-6}m^2$ in the lens and $1m^2$ throughout the rest of the domain, see Fig. 8). The flux boundary condition is $\mathbf{u}_N \cdot \mathbf{n} = -0.1m/s$ on the left boundary of the domain and the pressure on the right boundary is $p_D = 1000$ Pa. No flow boundary condition is imposed on the rest of the domain. The viscosity is the same as in Eq. 8. The time step is chosen as $\Delta t = 0.1$ s. The second-order method in space is employed. Through the remainder of the paper, we choose the IIPG method ($\epsilon_1 = 0$), as it reduces the complexity of discretization and flux reconstruction.

For the case without the flux reconstruction, the velocity on the face is given by

$$\mathbf{u}_h^{DG} = \{\mathbf{u}_h\}_\omega.$$

In Fig. 9, we observe a significant contrast for the concentration profile at $T = 8$ s if flux reconstruction is activated or not.

We can observe in Fig. 9 that the flux reconstruction reduces the non-physical oscillations around the region where the permeability changes. The effect is more obvious in the case of highly varying permeability. In the next numerical experiment, we use the permeability field from layer 39 of the SPE10 model [39]. The highly discontinuous permeability is shown in Fig. 10.

The flow is driven by injection and production wells: $\int_\Omega q^I = \int_\Omega q^P = 0.01m^2/s$. We inject from the lower left corner and produce from the upper right corner of domain. No flow boundary condition is imposed. The rest of the parameters is the same as in the previous experiment. Figure 11 demonstrates a clear improvement of the numerical concentration if flux reconstruction is activated. The case without flux reconstruction produces poor results with severe overshoot and undershoot.

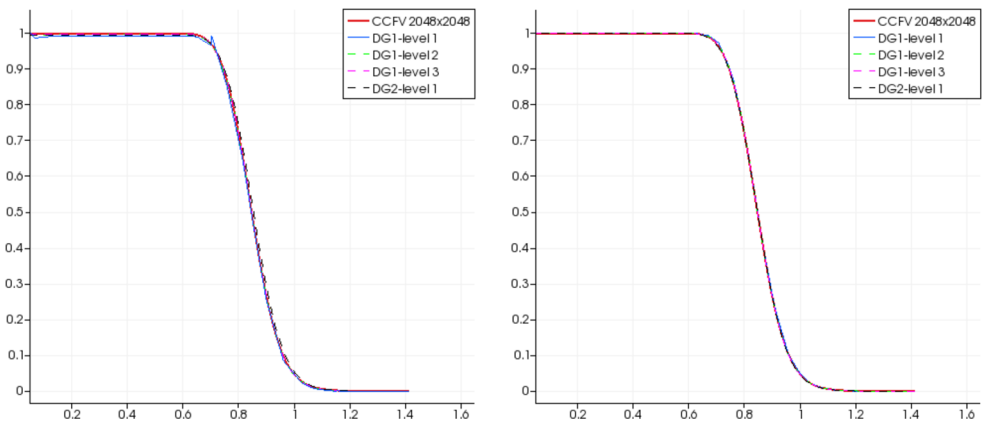

Fig. 22 Cross-section comparison: quadrilateral mesh (*left*) and triangular mesh (*right*)

We conclude this section by noting that, even for homogeneous porous media, solutions obtained with flux reconstruction are more accurate. We repeat the simple flux driven problem for a permeability equal to $1m^2$. Figure 12 compares the x-component velocity obtained with or without flux reconstruction at time $t = 0.8\ s$. In this homogeneous case, the exact velocity is $(0.1, 0)$. We observe a non-negligible error in the velocity without flux reconstruction. The error is larger at the location of the concentration front and arises from the coupling between the Darcy and transport systems.

6.3 Grid orientation effect

In subsurface modeling, the complex geological formations can be too complicated to be appropriately approximated by structured grids. On the other hand, unstructured grids, although they can more vividly portrait the geological formations, are likely to yield grid distortions. In the following numerical experiments, we evaluate the quality of the DG discretization when using distorted unstructured grids.

We consider the quarter five-spot problem illustrated in Fig. 13.

We consider injection and production rates given by $\int_\Omega q^I = \int_\Omega q^P = 0.18m^2/s$ and no flow boundary condition. The permeability is homogeneous ($1m^2$) and viscosity is set to be the same as Eq. 8. Our first test case is to consider grid distortion of 30° and −30°. The meshes that we use to test our method are shown in Fig. 14. The experiment is based on a numerical experiment conducted in [2].

We compare the solutions obtained with our DG method of first order (DG1) to the solutions obtained with the cell-centered finite volume (CCFV) method. It is well known that CCFV is not consistent on grids that are not k-orthogonal. Therefore, we also compute a reference CCFV solution on a 2048×2048 undistorted k-orthogonal grid. We

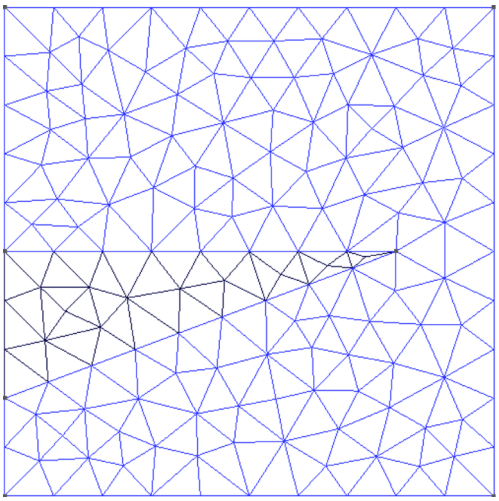

Fig. 24 Unstructured mesh for pinch-out example

first compare the concentration profiles at time $t = 0.5\ s$ on the grid with 30° distortion.

We observe in Fig. 15 that the DG solution is not sensitive to the grid distortion and can represent the reference solution well, which is to be expected since the DG method remains consistent on general arbitrary grids. Similar conclusions can be made from the comparisons on grid with −30° distortion, shown in Fig. 16.

We now test the quality of the DG solutions obtained on quadrilateral and triangular meshes given in Fig. 17.

Figures 18 and 19 show convergence of the DG solutions using h-refinement.

Figures 20 and 21 show convergence of the DG solutions using p-refinement. Solutions are computed on coarse meshes shown in Fig. 17.

We also plot the cross-section along the line with $y = x$ in Fig. 22 for the first-order method on several meshes

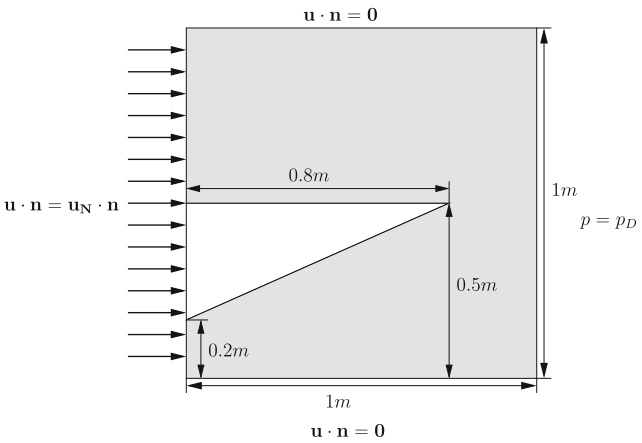

Fig. 23 pinch-out problem set-up and unstructured grid

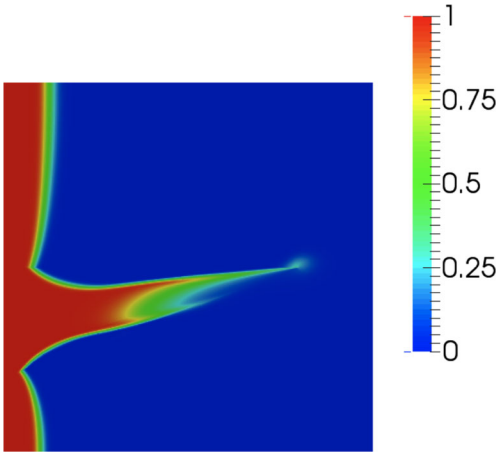

Fig. 25 Concentration profiles

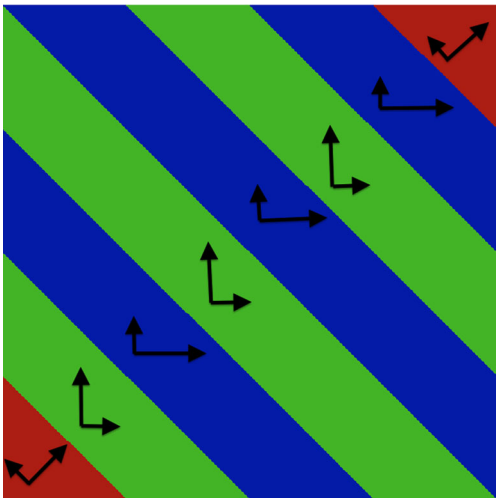

Fig. 26 Anisotropic permeability set-up

(level 1 to 3), and for the second-order method on the mesh of level 1. We observe that all curves coincide for the triangular meshes, whereas there are some small differences for the rectangular meshes, in particular with the first-order method on the mesh of level 1. Figure 22 also shows that there is no violation of the maximum principle. The grid Peclet number is 10^4 for the mesh of level 3, and 10^5 for the mesh of level 1.

Figure 22 demonstrates the accuracy of the DG solution in comparison with the reference solution by CCFV. Also, we observe the overshoot resulting from DG discretization, but it was reduced under hp-refinement.

Unstructured grid can better capture the complex geological formation as we will demonstrate in the next experiment that models a pinch-out geological formation. In Fig. 23, the pinch-out is the white triangular region with high permeability of $1m^2$, and the shaded region has low permeability $10^{-10}m^2$.

Flow is driven by boundary conditions, identical to the ones in Fig. 8. In order for CCFV to provide accurate solutions, we have to use k-orthogonal grid such as Cartesian grid. But, for this problem, the k-orthogonal grid simply fails to capture the realistic geometry around the pinch-out location. The flexibility of DG methods is an advantage for this particular set-up and enables us to both attain accurate geometry and solution accuracy. The unstructured grid that we use to realistically represent the geometry is illustrated in Fig. 24.

The concentration profile obtained by DG at time $t = 0.3s$ is shown in Fig. 25. The second-order DG solutions are obtained on a mesh with three levels of refinement.

Throughout the test cases that we have conducted, we observe that the method we propose has low sensitivity with respect to grid distortion and can achieve convergence using h- and p-refinement on unstructured grids.

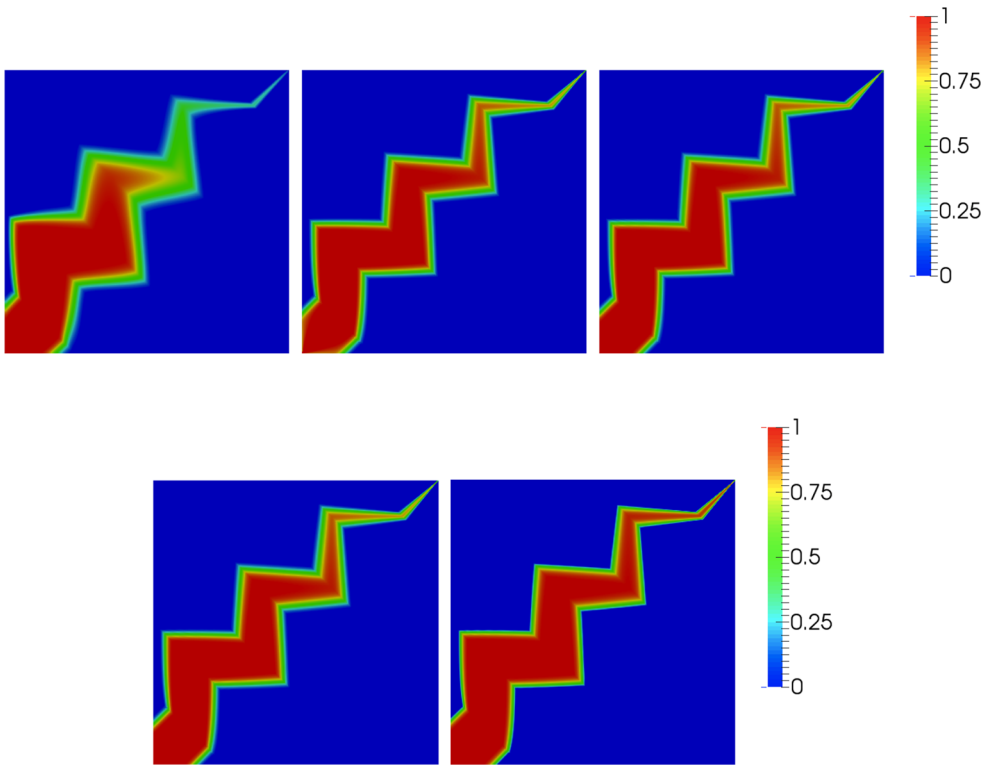

Fig. 27 Comparison between DG solutions for anisotropic medium: degree 1, 2, 3, 4, and 5

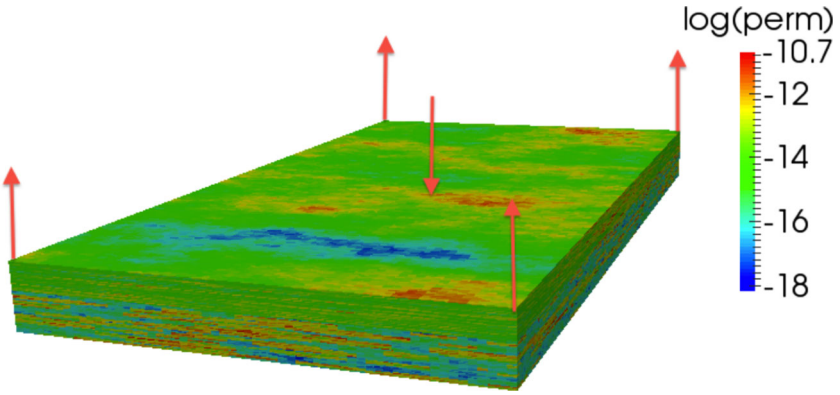

Fig. 28 SPE10 permeability and location of wells

6.4 Anisotropy permeability

Another important aspect when incorporating realistic geological model for the simulation in porous media is the anisotropy of the permeability.

To test the numerical method's ability to produce correct solution for anisotropic permeability field, we consider the same model problem as in Fig. 13 with the same input data except for permeability. Let $\mathbf{R}(\theta)$ denote the rotation matrix of angle θ. The permeability is defined as

$$\mathbf{k} = \mathbf{R}(-\theta) \begin{pmatrix} 100 & 0 \\ 0 & 1 \end{pmatrix} \mathbf{R}(\theta).$$

Figure 26 shows the spatial distribution of the permeability field; the angle θ is equal to 45° in the red regions and alternates between 90° and 0° in the green and blue regions. This experiment is based on a numerical experiment done in [2].

Figure 27 shows the concentration profiles obtained on a Cartesian grid of size 256×256 at time $0.25s$. We increase the polynomial degree from one to five. We note that as the polynomial degree increases the DG solution has less numerical diffusion. With the first-order DG method, the channel flow is captured but with some amount of numerical diffusion. In contrast, differences between the profiles obtained with DG of order two to five are negligible or very small.

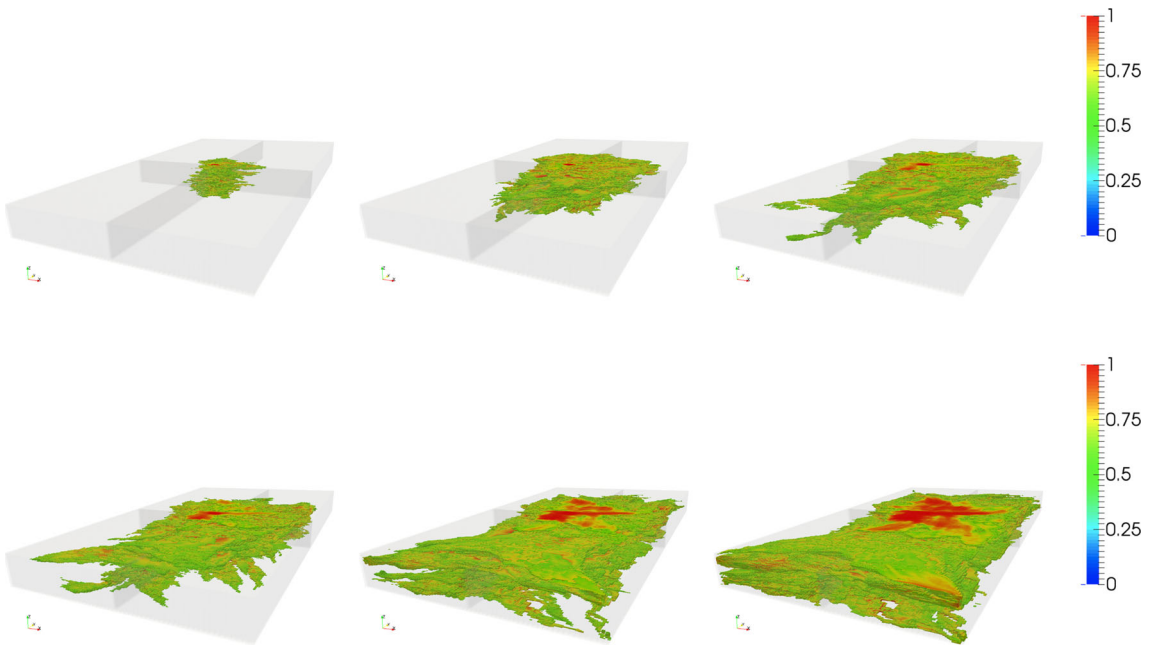

Fig. 29 Concentration snapshots obtained with DG2: 1, 5, 8, 10, 15, 20 days

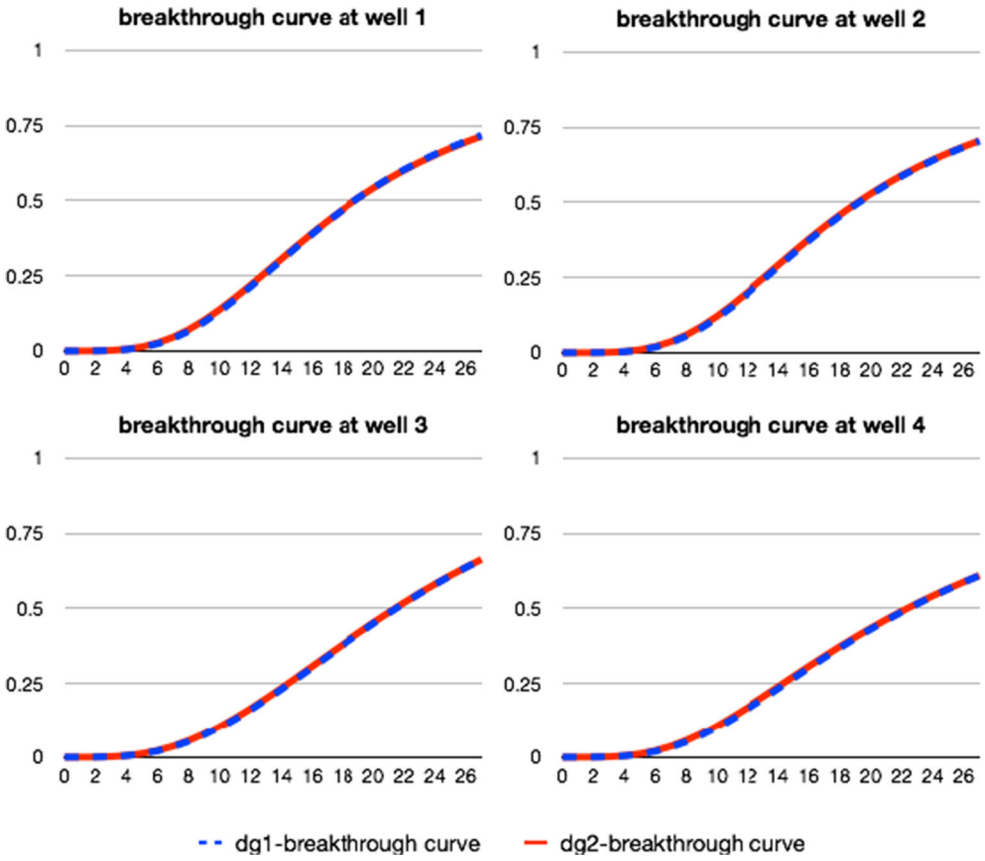

Fig. 30 Breakthrough curves at the production wells

6.5 Three-dimensional heterogeneous medium

The experiments we have done so far have demonstrated the robustness of the DG discretization while facing several numerical challenges. Next, we would like to test our discretization on some realistic physical data. We select the permeability field from the SPE10 model, which is well known for its large heterogeneities varying from $10^{-10}m^2$ to $10^{-18}m^2$. In addition, the bottom 50 layers of the permeability field represent the Upper Ness structure which includes underground channels that pose additional challenges. However, for simplicity, we assume the medium is isotropic and we keep the permeability in the z-direction the same as in the xy-direction.

We consider the five-spot problem by placing injection and production wells as in Fig. 28.

We set the injection rate to be $\int_\Omega q^I = 1.7\ m^3/s$ and production rate at each corner to be $\int_\Omega q^P = 0.425\ m^3/s$. Gravitational force $\mathbf{g} = (0, 0, -9.8)^T m/s^2$ is incorporated in the simulation. No flow boundary condition is imposed. Viscosities are

$$\mu_s = 10^{-3}\,Pa \cdot s \text{ and } \mu_o = 9 \times 10^{-4}\,Pa \cdot s.$$

Densities are

$$\rho_s = \rho_o = 1000\,kg/m^3.$$

We set a uniform time step to be 1 day and use piecewise quadratic approximation. The mesh consists of 1,220,000 elements. The Darcy system has 32,940,000 degrees of freedom ($\mathbb{Q}_2$) and the transport system 12,220,000 degrees of freedom ($\mathbb{P}_2$). Snapshots of the concentration profiles over several days are shown in Fig. 29. Concentrations are plotted above a threshold of 0.5. Even though we cannot theoretically guarantee a maximum principle, we observe that the numerical concentrations remain bounded between 0 and 1.

We observe in Fig. 29 that the simulation results can realistically represent the channels in the bottom layer of the Upper Ness structure. To validate our simulation result, we plot in Fig. 30 the average of the concentration at the production well over time. This curve is referred to as the breakthrough curve. We use the first- and second-order methods.

We observe in Fig. 30 that the breakthrough curves coincide. The plots give us confidence that the DG discretization can produce reliable results for large scale simulations.

7 Conclusion

In this paper, we have introduced a high-order discontinuous Galerkin method with weighted average stabilization and Raviart-Thomas flux reconstruction for solving the miscible displacement equations. Sequential decoupling approaches we employ maintain high-order convergence rate in time. The resulting linear system is implemented on parallel clusters using domain decomposition and solved using AMG preconditioner. A series of numerical experiments demonstrate the robustness and accuracy of the numerical method. Apart from the specific challenges in miscible displacement problem, the study of single-phase flow is the foundation for understanding multi-phase and multi-component flow problems in porous media. More work is needed to be able to apply our method to multi-phase and multi-component flow in porous media.

Acknowledgments This work was partially supported by NSF-DMS 1318348

References

1. Todd, M., O'dell, P., Hirasaki, G., et al.: Methods for increased accuracy in numerical reservoir simulators. Soc. Pet. Eng. J. **12**(06), 515–530 (1972)
2. Nikitin, K., Terekhov, K., Vassilevski, Y.: A monotone nonlinear finite volume method for diffusion equations and multiphase flows. Comput. Geosci., 1–14 (2013)
3. Palagi, C.L., Aziz, K.: Use of Voronoi grid in reservoir simulation. SPE Adv. Tech. Ser. **2**, 69–77 (1994)
4. Riviere, B., Wheeler, M.F.: Discontinuous Galerkin methods for flow and transport problems in porous media. Commun. Numer. Methods Eng. **18**(1), 63–68 (2002)
5. Rankin, R., Riviere, B.: A high order method for solving the black-oil problem in porous media. Adv. Water Resour. **78**, 126–144 (2015)
6. Li, J., Riviere, B.: Numerical solutions of the incompressible miscible displacement equations in heterogeneous media. Comput. Methods Appl. Mech. Eng. **292**, 107–121 (2015)
7. Rivière, B., Wheeler, M.: Discontinuous Galerkin methods for flow and transport problems in porous media. Commun. Numer. Methods Eng. **18**, 63–68 (2002)
8. Epshteyn, Y., Rivière, B.B.: Convergence of high order methods for miscible displacement. Int. J. Numer. Anal. Model. **5**, 47–63 (2008)
9. Bastian, P., Rivière, B.: Superconvergence and H(div) projection for discontinuous Galerkin methods. Int. J. Numer. Methods Fluids **42**(10), 1043–1057 (2003)
10. Scovazzi, G., Huang, H., Collis, S., Yin, J.: A fully-coupled upwind discontinuous Galerkin method for incompressible porous media flows: High-order computations of viscous fingering instabilities in complex geometry. J. Comput. Phys. **252**, 86–108 (2013)
11. Huang, H., Scovazzi, G.: A high-order, fully coupled, upwind, compact discontinuous Galerkin method for modeling of viscous fingering in compressible porous media. Comput. Methods Appl. Mech. Eng. **263**, 169–187 (2013)
12. Sun, S., Wheeler, M.F.: Discontinuous Galerkin methods for coupled flow and reactive transport problems. Appl. Numer. Math. **52**(2), 273–298 (2005)
13. Bartels, S., Jensen, M., Müller, R.: Discontinuous Galerkin finite element convergence for incompressible miscible displacement problems of low regularity. SIAM J. Numer. Anal. **47**(5), 3720–3743 (2009)
14. Jensen, M., Müller, R.: Stable Crank–Nicolson discretisation for incompressible miscible displacement problems of low regularity. Numerical Mathematics and Advanced Applications, 469–477 (2010)
15. Li, J., Riviere, B., Walkington, N.: Convergence of a high order method in time and space for the miscible displacement equations. ESAIM: Mathematical Modelling and Numerical Analysis **49**, 953–976 (2015)
16. Luo, Y., Feng, M., Xu, Y.: A stabilized mixed discontinuous Galerkin method for the incompressible miscible displacement problem. Boundary Value Problems **2011**(1), 1–17 (2011)
17. Ern, A., Stephansen, A.F., Zunino, P.: A discontinuous Galerkin method with weighted averages for advection–diffusion equations with locally small and anisotropic diffusivity. IMA J. Numer. Anal. **29**(2), 235–256 (2009)
18. Ern, A., Nicaise, S., Vohralík, M.: An accurate H(div) flux reconstruction for discontinuous Galerkin approximations of elliptic problems. Comptes Rendus Mathematique **345**(12), 709–712 (2007)
19. Bastian, P.: Higher order discontinuous Galerkin methods for flow and transport in porous media. Lecture Notes in Computational Science and Engineering **35**, 1–22 (2003)
20. Ern, A., Mozolevski, I., Schuh, L.: Discontinuous Galerkin approximation of two-phase flows in heterogeneous porous media with discontinuous capillary pressures. Comput. Methods Appl. Mech. Eng. **199**(23), 1491–1501 (2010)
21. Ern, A., Mozolevski, I., Schuh, L.: Accurate velocity reconstruction for discontinuous Galerkin approximations of two-phase porous media flows. Comptes Rendus Mathematique **347**(9), 551–554 (2009)
22. Arbogast, T., Juntunen, M., Pool, J., Wheeler, M.F.: A discontinuous Galerkin method for two-phase flow in a porous medium enforcing H(div) velocity and continuous capillary pressure. Comput. Geosci. **17**(6), 1055–1078 (2013)
23. Bastian, P., Blatt, M., Scheichl, R.: Algebraic multigrid for discontinuous Galerkin discretizations of heterogeneous elliptic problems. Numerical Linear Algebra with Applications **19**(2), 367–388 (2012)
24. Blatt, M.: A parallel algebraic multigrid method for elliptic problems with highly discontinuous coefficients, Ph.D. thesis. University of Heidelberg (2010)
25. Dobrev, V.A., Lazarov, R.D., Vassilevski, P.S., Zikatanov, L.T.: Two-level preconditioning of discontinuous Galerkin approximations of second-order elliptic equations. Numerical Linear Algebra with Applications **13**, 753–770 (2006)
26. Van Slingerland, P., Vuik, C.: Fast linear solver for diffusion problems with applications to pressure computation in layered domains. Comput. Geosci. **18**(3-4), 343–356 (2014)
27. Danilov, A., Vassilevski, Y.V.: A monotone nonlinear finite volume method for diffusion equations on conformal polyhedral meshes. Russ. J. Numer. Anal. Math. Model. **24**(3), 207–227 (2009)
28. Cockburn, B., Shu, C.-W.: TVB Runge-Kutta local projection discontinuous Galerkin finite element method for conservation laws. II. General framework. Math. Comput. **52**(186), 411–435 (1989)

29. Cockburn, B., Lin, S.-Y., Shu, C.-W.: TVB Runge-Kutta local projection discontinuous Galerkin finite element method for conservation laws III: one-dimensional systems. J. Comput. Phys. **84**(1), 90–113 (1989)
30. Hoteit, H., Ackerer, P., Mosé, R., Erhel, J., Philippe, B.: New two-dimensional slope limiters for discontinuous Galerkin methods on arbitrary meshes. Int. J. Numer. Methods Eng. **61**(14), 2566–2593 (2004)
31. Moissis, D.: Simulation of viscous fingering during miscible displacement in nonuniform porous media, Ph.D. thesis. Rice University (1988)
32. Koval, E.: A method for predicting the performance of unstable miscible displacement in heterogeneous media. Soc. Pet. Eng. J. **3**(02), 145–154 (1963)
33. Bastian, P.: A fully-coupled discontinuous Galerkin method for two-phase flow in porous media with discontinuous capillary pressure. Comput. Geosci. **18**(5), 779–796 (2014)
34. Ewing, R.E., Russell, T.F.: Efficient time-stepping methods for miscible displacement problems in porous media. SIAM J. Numer. Anal. **19**(1), 1–67 (1982)
35. Thomée, V.: Galerkin finite element methods for parabolic problems, Vol. 1054. Springer (1984)
36. Bastian, P., Blatt, M., Dedner, A., Engwer, C., Klöfkorn, R., Ohlberger, M., Sander, O.: A generic grid interface for parallel and adaptive scientific computing. part I: abstract framework. Computing **82**(2-3), 103–119 (2008)
37. Bastian, P., Blatt, M., Dedner, A., Engwer, C., Klöfkorn, R., Kornhuber, R., Ohlberger, M., Sander, O.: A generic grid interface for parallel and adaptive scientific computing. part II: Implementation and tests in DUNE. Computing **82**(2-3), 121–138 (2008)
38. Bastian, P., Heimann, F., Marnach, S.: Generic implementation of finite element methods in the distributed and unified numerics environment (DUNE). Kybernetika **46**(2), 294–315 (2010)
39. Website: http://www.spe.org/web/csp/datasets/set02.htm